ELSEVIER

Mechanics of Materials 33 (2001) 425–439

MECHANICS OF MATERIALS

www.elsevier.com/locate/mechmat

Dynamic response of conventional and hot isostatically pressed Ti–6Al–4V alloys: experiments and modeling

Sia Nemat-Nasser *, Wei-Guo Guo, Vitali F. Nesterenko, S.S. Indrakanti, Ya-Bei Gu

Department of Mechanical and Aerospace Engineering, Center of Excellence for Advanced Materials, University of California, San Diego, La Jolla, CA 92093-0416, USA

Received 1 February 2001; received in revised form 1 April 2001

Abstract

This paper presents the results of a systematic comparative study of the dynamic thermomechanical response of Ti–6Al–4V alloys with three different microstructures. Two of the alloys are produced by the hot isostatically pressed technique using rapidly solidified granules, with one alloy milled prior to hot pressing. Experiments are performed over a broad range of strain rates, 10^{-3}–7000 s^{-1}, and initial temperatures, 77–1000 K. Depending on the test temperature, compressive strains of 10–60% are achieved. The microstructure of the undeformed and deformed specimens is investigated, using optical microscopy. The dependence of the flow stress on the temperature and the strain rate is examined for various strains and it is related to the corresponding material microstructure. The results show that adiabatic shearbands develop at high strain rates, as well as at low strain rates and high temperatures. Depending on the test temperature, shearbands initiate once a sample is deformed to suitably large strains. The flow stress is more sensitive to temperature than to the strain rate. Based on these results and other published work, the thermally activated mechanisms associated with the dislocation motion are identified. The physically based model proposed by Nemat-Nasser and Li (1997) for OFHC copper, is suitably modified and applied to this class of titanium alloys. In the absence of dynamic strain aging, the model predictions are in good accord with the experimental results. Comparing the results for the three considered Ti–6Al–4V alloys, with different microstructures, it is found that the initial microstructural features affect only the magnitude of the threshold stress and the athermal part of the flow stress, but not the functional dependence of the thermally activated part of the flow stress on the temperature and the strain rate.

Keywords: Ti–6Al–4V; Hot isostatic pressing; Flow stress; Strain rate; Microstructure; Modeling

1. Introduction

Titanium, an allotropic element, exists as a hexagonal close-packed (hcp) crystal at room temperature, referred to as the α-Ti, and as a body-centered cubic (bcc) crystal, referred to as the β-Ti, at 1100 K. Through the addition of alloying elements, the α or β phase is stabilized. Aluminum and vanadium are the most common α and β stabilizers, respectively. Below the β transus temperature, the titanium alloy is a mixture of α and β phases, when the alloying involves α and β stabilizers. Ti–6Al–4V (hereinafter referred to as

* Corresponding author. Tel.: +1-858-534-4914; fax: +1-858-534-2727.

E-mail address: sia@shiba.ucsd.edu (S. Nemat-Nasser).

0167-6636/01/$ - see front matter
PII: S0167-6636(01)00063-1

Ti64), as a typical $\alpha + \beta$-type alloy, is the most widely used titanium alloy, due to its attractive specific strength and corrosion resistance. It however, generally contains impurity elements which affect its thermomechanical properties.The microstructure of this alloy is strongly influenced by the processing history and the heat treatment. Furthermore, its mechanical properties are dictated by the initial microstructure, the thermomechanical loading history, and the impurities, such as interstitials (especially oxygen) (Montgomery et al., 1997), which can be used to optimize the dynamic performance of the alloy (Burkins and Love, 1996; Me-Bar and Rosenberg, 1997). In the present work, we seek to examine experimentally, the effect of the strain rate, temperature, and the initial microstructure on the mechanical properties of Ti64, and to develop a physically based model which can predict the response of this material at high strain rates and various temperatures.

Currently, extensive experimental results at low strain rates for titanium alloys of various microstructures are available (Doner and Conrad, 1973; Okazaki et al., 1974; De Meester et al., 1975; Kerr, 1985; McDarmaid and Partridge, 1986; Makel and Eylon, 1990; Kailas et al., 1994), revealing many interesting characteristics of these materials. For example, Conrad and coworkers (Doner and Conrad, 1973; Okazaki et al., 1974) in their study of the commercial titanium Ti-50A (0.5 at.% pct O_{eq}) and Ti–7.4 at.% Al alloys, conclude that the thermal activation parameters for the plastic deformation of these alloys are the same as those of the unalloyed titanium, and that the dominant rate-controlling mechanism in these materials is the thermally activated process of dislocations overcoming their obstacles which may include interstitial solute atoms. They further show that dynamic strain aging occurs in the temperature range, 600–850 K, for Ti-50A. The grain size (1–12 μm) in the Ti–7.4 at.% Al alloy, primarily influences the athermal part of the flow stress. In contrast to the low-strain rate studies, less attention has been given to the high-strain rate properties of titanium alloys. The deformation substructure observed in Ti64, consists of planar slip in the α grains, at quasi-static strain rates, while at high strain rates deformation twinning is also observed (Follansbee and Gray, 1989). In general, adiabatic shearbanding occurs after suitable straining accompanied by high dislocation density (Me-bar and Shechtman, 1983). A study by Lee and Lin (1998) shows that at high strain rates, Ti64's temperature sensitivity increases with the temperature. The susceptibility to shearbanding of Ti64, generally leads to inhomogeneous deformation, instability and even local melting at high strain rates, and finally, to fracture (Makel and Eylon, 1990). This type of fracturing is typically encountered in ballistic impact, producing plugging in relatively thick Ti and Ti64 targets (Grebe et al., 1985). Understanding of dynamic properties and critical conditions for shear localization is important in, for example, the improving ballistic performance of these materials (Nesterenko et al., 2000).

2. Experimental procedure

2.1. Material

Three different processing techniques are involved in producing Ti64 alloys of three different microstructures, considered in the present work. The first material is a commercial Ti64 alloy rod (MIL-T-9047G), 25.4 mm in diameter, purchased from Protech Metals. The second material, designated RS-MIL-HIP, and the third material, designated RS-HIP, are produced by hot isostatic pressing (HIP), as described below.

Hot isostatic pressing is an efficient technique to produce high quality materials from powders. Rapidly solidified PREP Ti64 spherical powder, obtained from Nuclear Metals, is used in this investigation. In one case, the powder is milled for 10 min in a SPEX 8000-impact ball mill in a tungsten carbide lined vessel, using tungsten carbide balls. The ball-to-powder weight ratio is 8:1. The milling process plastically deforms the initially spherical powder grains. In some cases welding of the powder particles occurs. The milled powder is then degassed in a vacuum (10^{-2} Torr) oven at 220°C for 10 h.

A 12.5 mm Pyrex glass capsule is filled halfway with the milled powder, and packed down by

vibration. The remainder of the capsule is packed with the spherical nonmilled powders to ensure an identical HIP cycle for both materials. The overall density of the powder is in the range of 58–60% theoretical. The capsules are sealed under vacuum. Then the sample is HIPed in QIH-3 miniHIPer (ABB autoclaves) at a temperature of 1050°C and a pressure of 200 MPa for 2 h. The capsules are initially heated above the glass-softening temperature to 850°C in about 45 min with a minimal pressure of <1 MPa (50–100 psi). After the temperature of 850°C is reached, the samples are kept at this constant temperature for 5 min before the pressure is raised to 165 MPa (24 000 psi) in about 20 min. The samples are brought to a temperature of 1050°C and pressure of 200 MPa for about 5–10 min. The main part of the HIPing cycle is carried out for 2 h at the desired temperature and at 200 MPa pressure. The cycle is optimized based on micromechanical modeling of the densification process (Liu et al., 1998). At the end of the process, the pressure and temperature are dropped to 1 MPa and 50°C in 30 min. The HIPed samples are cut to separate the milled and nonmilled portions. These are designated as RS-MIL-HIP and RS-HIP, respectively. The chemical compositions of the three alloys are given in Table 1.

The additional oxygen in the Ti64 increases the β transus temperature (Boyer et al., 1994). From the presented chemical analysis it is apparent that the RS-HIP material may have been in the β region, while the RS-MIL-HIP may have been in the $\alpha + \beta$ region during the HIPing at 1050°C.

Samples are analyzed for interstitial content (O, C, N and H) using the ASTM method. The chemistry of the powders remained the same for RS-HIPed material as it was for the starting powder: C – 0.01, N – 0.01, H – 0.002 and O – 0.18 wt%. The milling process itself results in an increase of O and C to 0.28 and 0.02 wt%, respectively. The subsequent HIPing does not change this interstitial content.

Cylindrical specimens, 5 mm in diameter and 5 mm in height, are machined from the three materials. The commercial Ti64 specimens are annealed at 748°C, for 1 h, in a vacuum of approximately 10^{-5} Torr, and then air-cooled to room temperature. The initial microstructure of each material is examined, using optical microscopy. For this, typical samples are first sectioned along the compression axis, polished, then etched in a solution of 2% HF, 10% HNO_3, and 88% H_2O, for about 3 min, before optical observation.

2.2. Compression tests

The low-strain rate tests at 10^{-3} and 10^{-2} s^{-1} strain rates, in the temperature range, 296–800 K, are performed using an Instron testing machine, equipped with a furnace with a high-intensity quartz lamp, and a ceramic loading fixture. The high-temperature tests are performed in an argon atmosphere and the temperature is maintained constant, to within ±2°C.

The high-strain rate tests, with 1000–7000 s^{-1} strain rates, and at 77–1000 K initial temperatures, are performed using UCSD's recovery Hopkinson bar facility, enhanced for high-temperature and high-strain rate recovery tests (Nemat-Nasser et al., 1991; Nemat-Nasser and Isaacs, 1997). The facility allows preheating a sample within a furnace, while the transmission and incident bars are kept outside the high-temperature zone. These bars are then automatically brought into gentle contact with the specimen, just before the stress pulse reaches the specimen end of the incident bar. The temperature of the specimen is measured by a thermocouple which holds the specimen inside the furnace. The reflected tensile pulse in the incident bar is trapped, so that the sample is subjected to a single compression pulse of desired profile, as

Table 1
Chemical composition of Ti64 alloy (wt%)

Materials	A	V	Fe	O	C	N	H	Y	Ti
Commercial	6.21	3.61	0.21	0.19	0.01	0.01	0.0006	<0.001	Bal.
RS-MIL-HIP	6.33	4.13	0.19	0.28	0.02	0.008	0.002	<0.005	Bal.
RS-HIP	6.33	4.13	0.19	0.2	0.01	0.008	0.002	<0.005	Bal.

discussed by Nemat-Nasser et al. (1991), who have developed the recovery Hopkinson technique.

3. Experimental results

3.1. Strain rate and temperature dependency

In Fig. 1(a)–(d), true stress–true strain relations are presented for the three materials at indicated strain rates and initial temperatures. Fig. 1(A) displays the adiabatic stress–strain curves for various strain rates and initial temperatures. The two low strain rate (10^{-3} s^{-1}) curves in Fig. 1(b) are essentially isothermal, while the curve at 6000 s^{-1} and initially room temperature, is adiabatic. The dotted curves are obtained at a 2000 s^{-1} strain rate and at initial room temperature, by interrupted tests of the same sample. Hence, the three dotted curves can be used to construct a quasi-isothermal room temperature stress–strain relation at a 2000 s^{-1} strain rate. As is seen from Fig. 1(a) and (b), the material's sensitivity is greater to the temperature than the strain rate. Fig. 1(c) and (d) show similar results for the other two titanium alloys. Again, greater temperature sensitivity than strain rate sensitivity is displayed.

3.2. Microstructural observation

Initial cold working of the powders modifies the microstructure of the resulting material. Examples of microstructures obtained prior to deformation are presented in Figs. 2(a)–(c). The microstructure of the RS-HIP material exhibits fine lamellar structure with prior β grain boundaries and typical

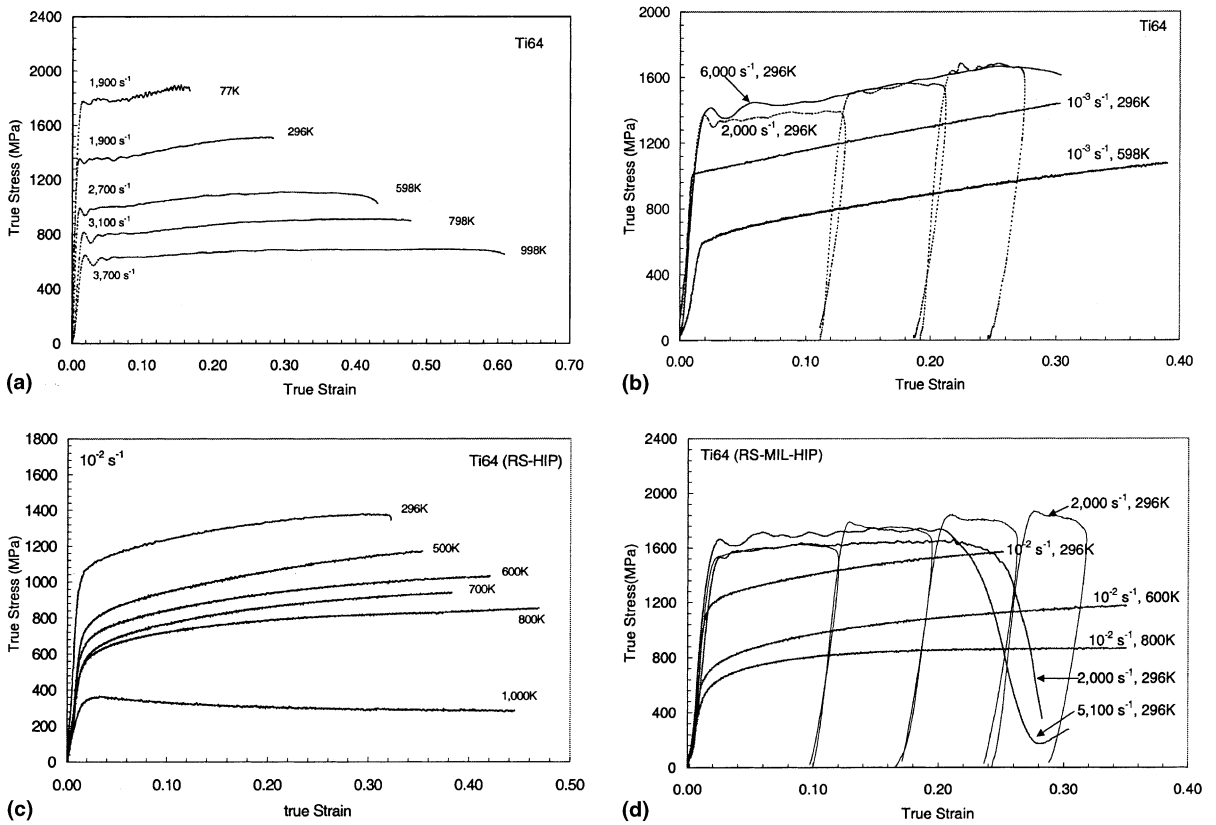

Fig. 1. Typical true stress–true strain curves of Commercial Ti64, RS-HIP Ti64 and RS-MIL-HIP Ti64 at indicated initial temperatures and strain rates.

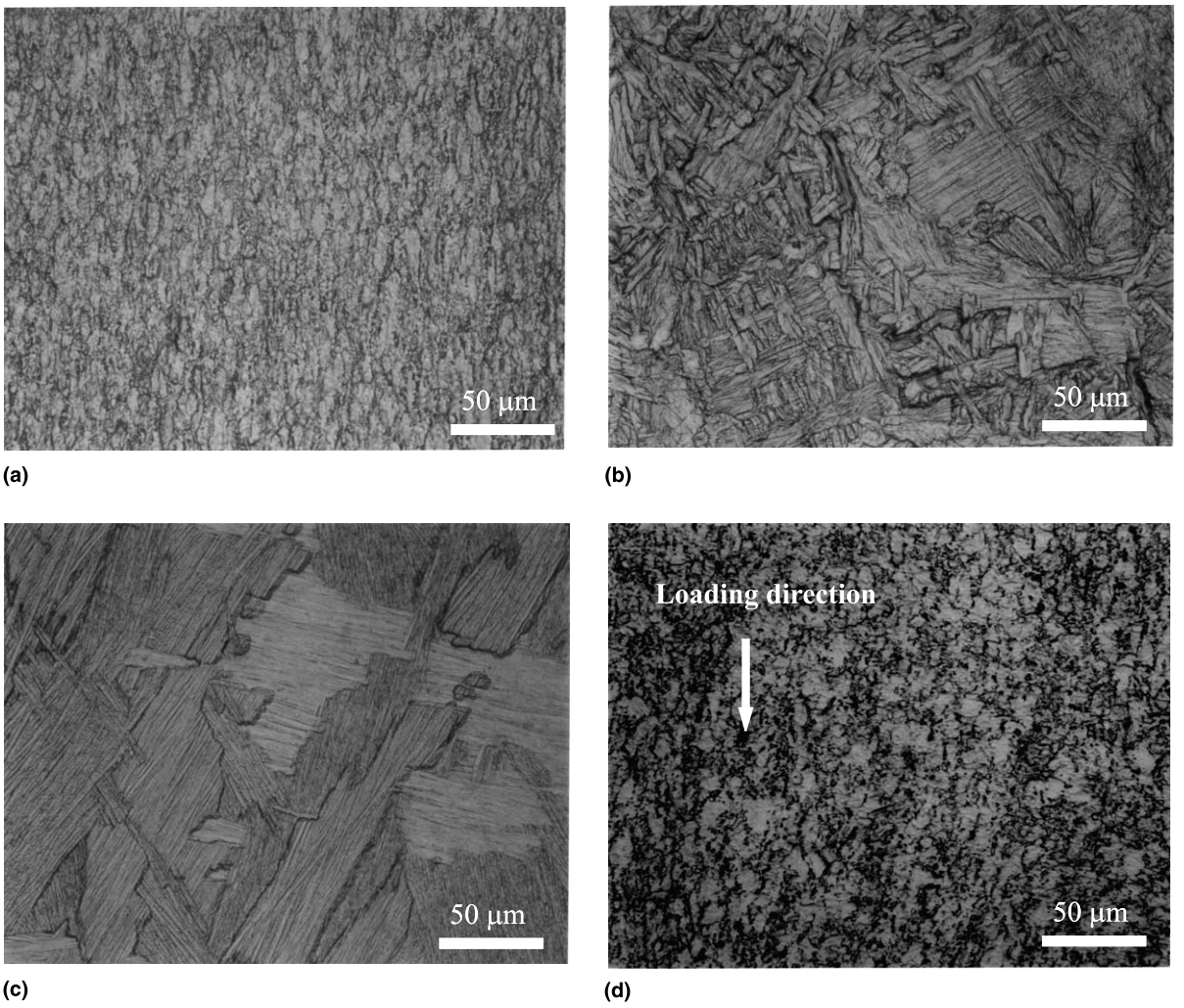

Fig. 2. (a)–(c) Microstructure of commercial RS-MIL-HIP and RS-HIP Ti64, respectively, before testing, (d) microstructure of commerical Ti64 at 600 K, 10^{-3} s^{-1} and a strain of 0.45.

Widmanstatten pattern of $\alpha + \beta$ (Fig. 2(c)). The grains in RS-MIL-HIP are more equiaxed with an average size of 7 μm (Fig. 2(b)). Some regions of lamellar structure in particles less deformed during milling, are also noticeable in parts of the material.

The circular cylindrical samples have been sectioned (after deformation) along the cylindrical axis that constitutes the loading direction for all the samples. Fig. 2(d) shows the microstructure of the commercial Ti64, tested at a 10^{-3} s^{-1} strain rate and 600 K temperature, to a strain of 0.45. As is seen from Figs. 2(b) and (c), the microstructures of RS-MIL-HIP and RS-HIP Ti64 are considerably different than the microstructure of the commercial alloy. Such variations in the microstructure seem to affect the initial yield stress and the athermal part of the flow stress, but not the functional form of the thermally activated part, as will be shown later on. This should be expected, since the gross microstructural features shown in Fig. 2 do not affect the dislocation–dislocation interaction in a thermally activated mechanism. We have observed the failure modes of these materials, as summarized below.

Commercial Ti64: Depending on the temperature and, to some extent, the strain rate, this material fails by shearbanding, leading to fracture, as illustrated in Fig. 3. In general, titanium alloys have low thermal conductivity which, however, increases with increasing temperature. For example, Ti64's thermal conductivity changes from about 7 W m^{-1} K^{-1} at 20°C, to about 17 W m^{-1} K^{-1} at 815°C (Williams, 1965; ASM Metal Handbook, 1980). Therefore, high-strain rate deformation at low temperatures promotes shearbanding. As is seen from the microstructures of Fig. 3, even at a 1000 K initial temperature, shearbands develop in the sample deformed to a true strain 0.6, at a 3700 s^{-1} strain rate (see Fig. 3(a)). At an initial room temperature, sharp shearbands are seen to have developed at strain rates of 6000 and 1900 s^{-1}. As shown in Figs. 3(b) and (c), even for much smaller total strains, melting has occurred in the shearband of Fig. 3(b) which also shows voids that are formed during the deformation. Fig. 3(d) shows the fracture surface resulting from the adiabatic shearbanding. The smooth portion of this surface corresponds to the shear zone that is flanked by two tension zones.

RS-MIL-HIP and RS-HIP Ti64: The other two materials as shown in Figs. 4 and 5 display frac-

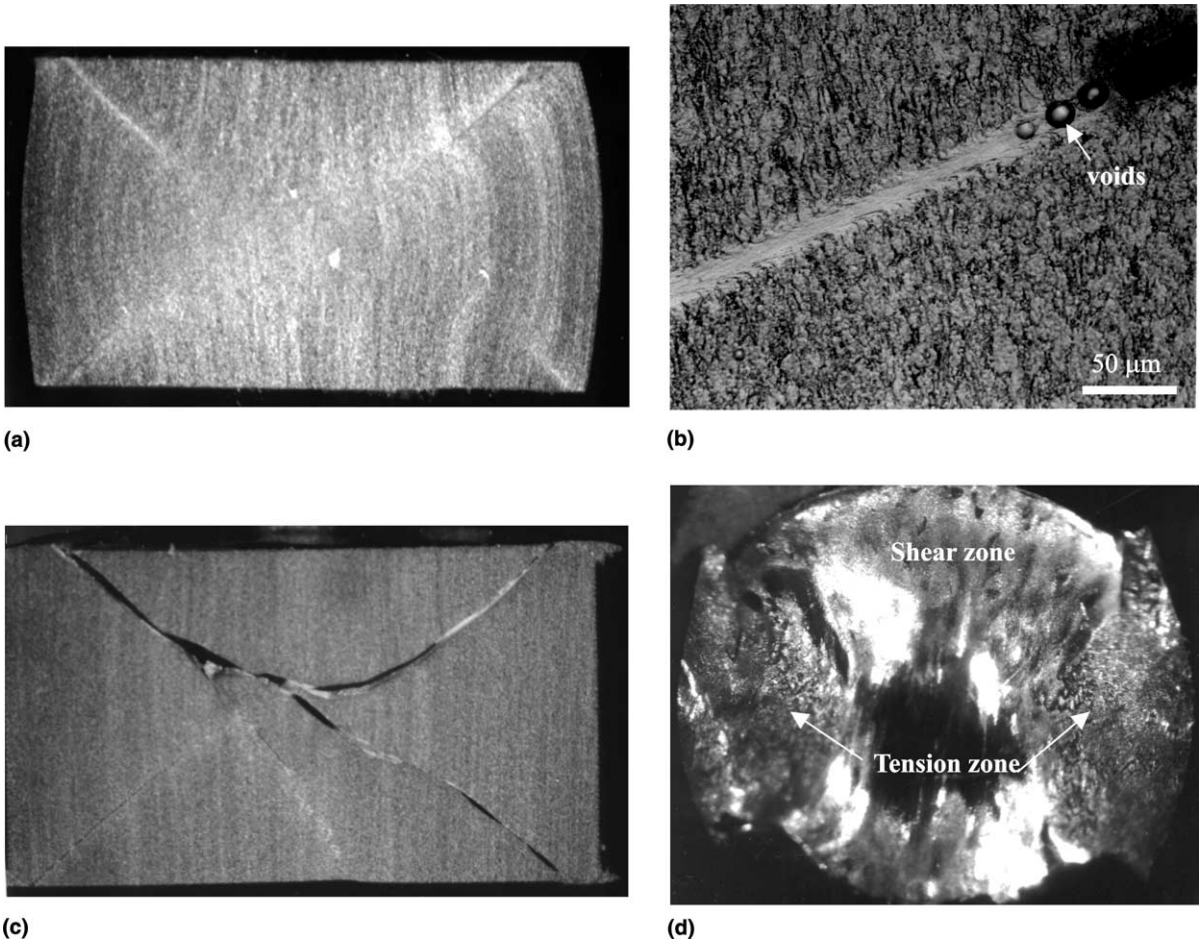

Fig. 3. Adiabatic shearband and fracture features of commercial Ti64, (a) at 1000 K, 2000 s^{-1} and a true strain of 0.6, (b) and (c) at 296 K, 6000 s^{-1} and a true strain of 0.35, (d) fracture surface at 296 K, 1900 s^{-1}.

tures similar to the commercial Ti64. The microstructure of RS-MIL-HIP Ti64 deformed quasi-statically to about 0.45 true strain, at 800 K and a of 10^{-2} s^{-1} strain rate, is shown in Fig. 4(a), and that of RS-HIP Ti64 deformed to the same strain at 1000 K and the same strain rate, is shown in Fig. 5(a). Comparing these with Fig. 2(c) and (d), it is seen that the deformation alters the coarse microstructural features of these two materials. The grains are elongated along a 45° axis, suggesting that further deformation might have led to strain localization, even at such high-temperatures. The room temperature experiments at 2000 s^{-1}, to slightly over 0.20 strain, have produced shearbands, as is seen in these figures. It is also interesting to note that the deformation has changed the grain structure to more or less equiaxed grains (recrystallization). Furthermore, adiabatic shearbands develop and voids are created, outside the shearbands.

The response of RS-HIP Ti64 is similar to that of RS-MIL-HIP Ti64. The high-strain rate, room

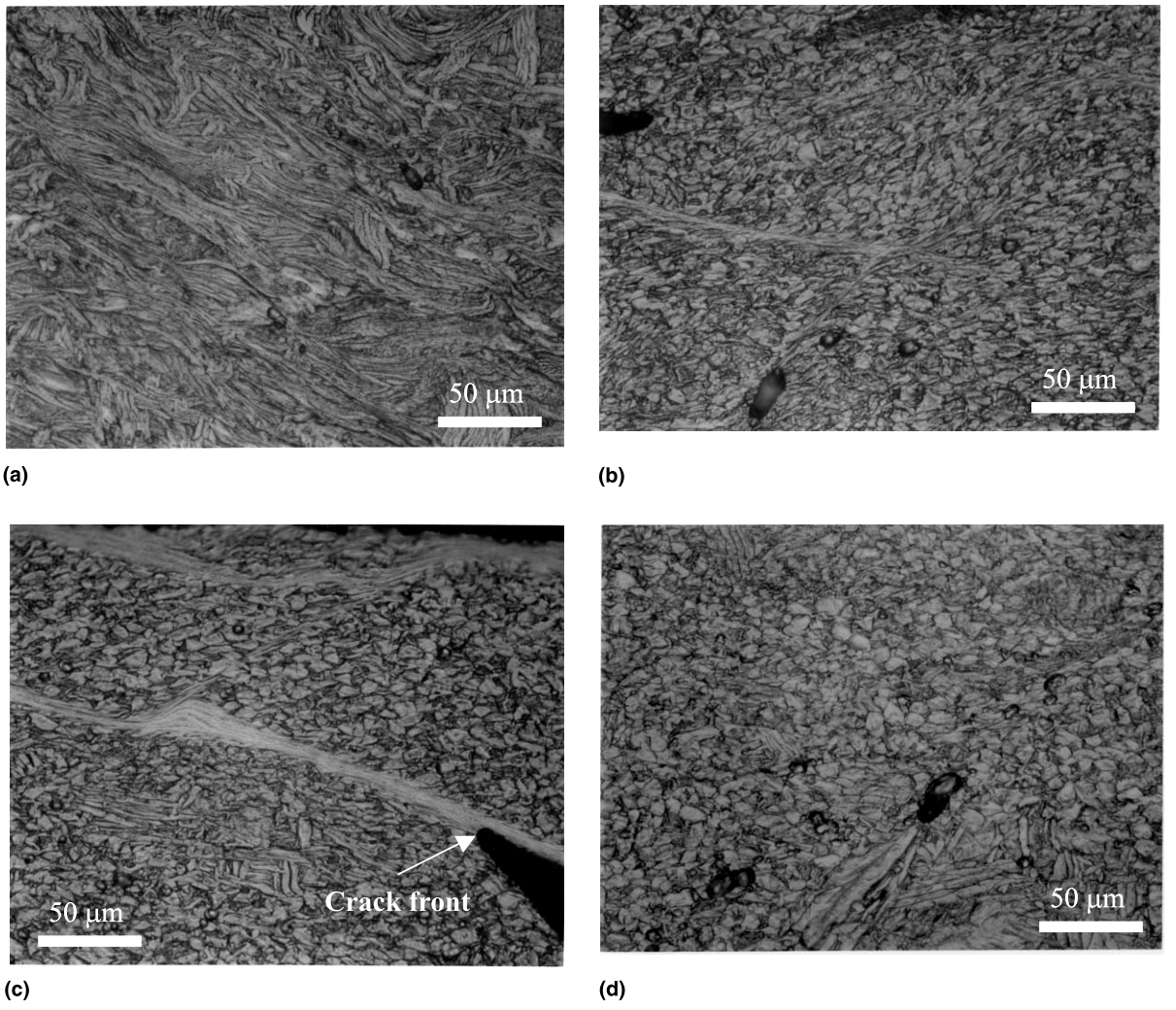

Fig. 4. Optical micrographs of adiabatic shearband and fracture of RS-MIL-HIP Ti64, (a) at 800 K, 10^{-2} s^{-1} and a true strain of 0.45, (b) to (d) at 296 K, 2000 s^{-1} and a strain of 0.24.

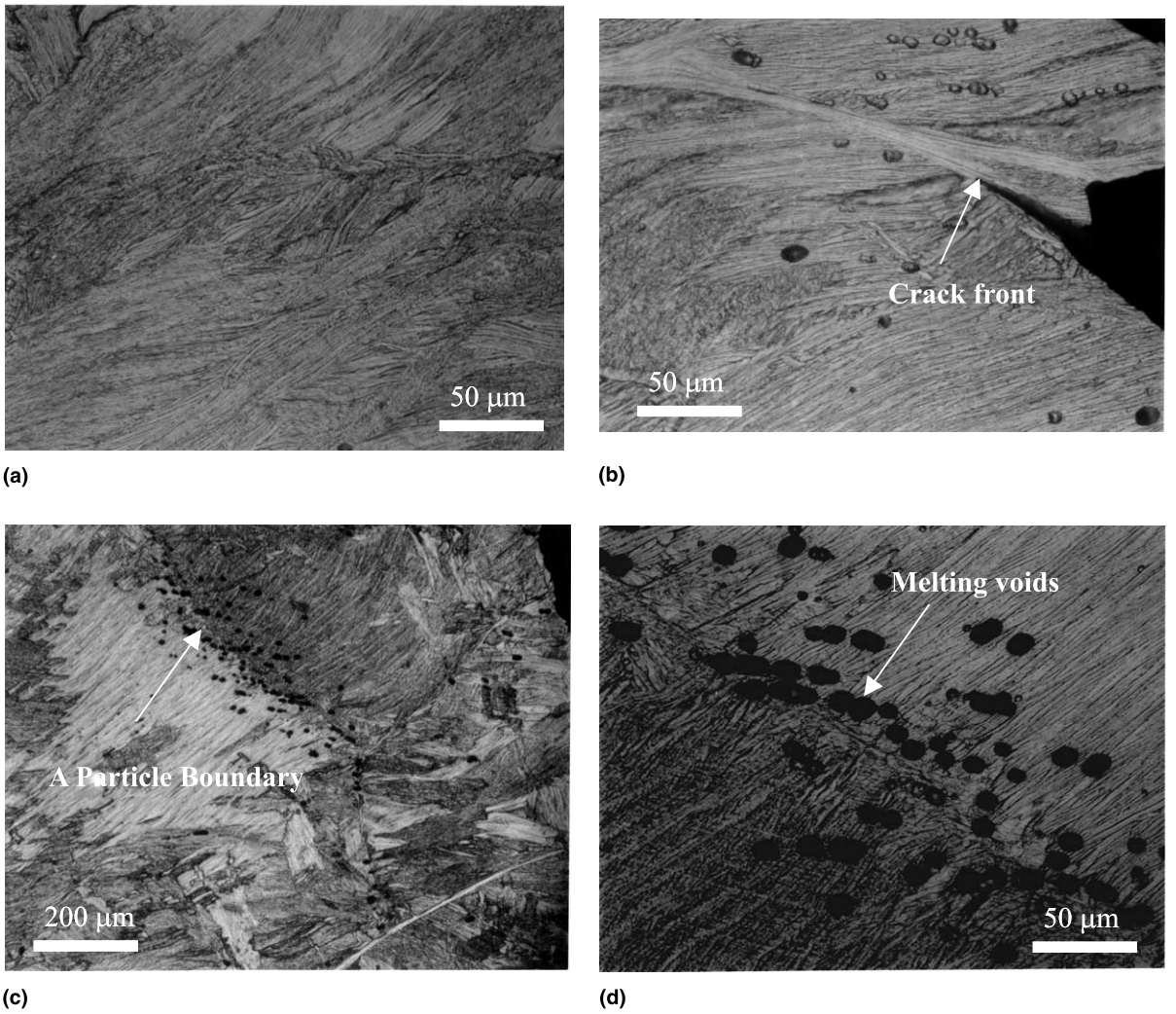

Fig. 5. Optical micrographs of adiabatic shearband and fracture of RS-HIP Ti64, (a) at 1000 K, 10^{-2} s^{-1} and a true strain of 0.45, (b) to (d) at 296 K, 2400 s^{-1} and a strain of 0.22.

temperature tests produce localized deformation, for strains exceeding 0.20. The adiabatic shearbands are formed in this case along the grain boundaries, suggesting a relatively weak bonding between the large grains. Numerous voids due to melting are also observed. They occur mostly in the vicinity of the grain boundaries which have poor conductivity.

In general, it can be concluded that the hot isostatically pressed material's fracturing mode is similar to that of the conventional alloy.

4. Temperature and strain rate effects on flow stress

As is shown, all three materials are highly temperature sensitive, and their shearbanding propensity is strongly temperature-dependent and weakly strain-rate-dependent. In an adiabatic straining, the temperature rise is calculated from

$$\Delta T = \int_0^{\gamma} \frac{\eta}{\rho' C_{\mathrm{V}}} \tau \, \mathrm{d}\gamma, \tag{1}$$

where ρ' is the mass density (4.39 g/cc), C_V is the heat capacity at constant volume, and η is the fraction of the plastic work converted to heat and used to raise the temperature of the sample. For Ti64 alloys, the temperature dependence of C_V must be included in the calculation, since C_V can change from 0.58 J g^{-1} K^{-1} at 20°C, to 0.93 J g^{-1} K^{-1} at 870°C (ASM Metal Handbook, 1980). A good approximation of this temperature dependence over the considered temperature range, is given by $C_V = 0.56\ \exp(T/2000)$, obtained through fitting the actual data.

It has been shown by Nemat-Nasser et al. (1994); Nemat-Nasser and Isaacs (1997); and Kapoor and Nemat-Nasser (1998) and carefully confirmed by Kapoor and Nemat-Nasser (1998) that, at high strain rates, essentially all the plastic work can be assumed to be converted into heat, for strains exceeding a few percent. Fig. 6(a) verifies this. A sample of commercial Ti64 has been loaded at a 2000 s^{-1} strain rate and an initial temperature of 325°C, to about 0.17 strain. Then the sample has been cooled to room temperature, subsequently heated to 387°C, and reloaded at the same 2000 s^{-1} strain rate. According to Eq. (1), the increase of 62°C corresponds to $\eta = 1$, i.e., when all the plastic work is used to increase the temperature of the sample. As is evident from Fig. 6(a), the assumption of $\eta \approx 1$ is good within experimental error.

Fig. 6(b) displays the flow stress of commercial Ti64 as a function of temperature, T, which is calculated using Eq. (1) and $T = T_0 + \Delta T$, T_0 being the initial temperature of the sample. Fig. 6(c) gives the flow stress of RS-HIP Ti64 for a strain rate of 10^{-2} s^{-1}, and the indicated strains. These data suggest the presence of slight dynamic strain aging, occurring in the range of temperatures

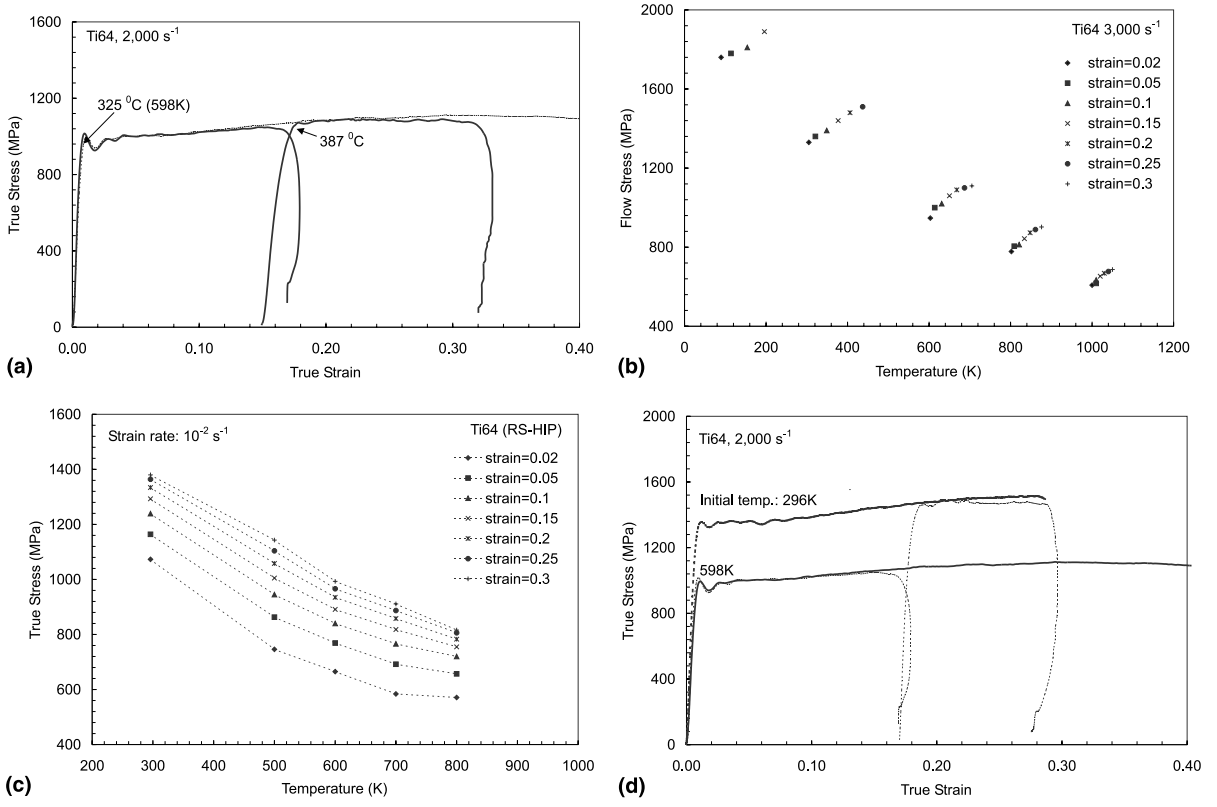

Fig. 6. (a) Verification of converting the plastic work into heat; flow stress as a function of temperature (b) for commercial Ti64, (c) RS-HIP Ti64, and (d) interrupt test for commercial Ti64.

from 500 to 800 K, in agreement with the results of Doner and Conrad (1973) and Reed-Hill et al. (1996). In general, dynamic strain aging is explained based either on an impurity drag model [drag of Cottrell atmosphere by dislocations (Cottrell and Jaswon, 1949; Keh et al., 1968)], or on an impurity pinning model (pinning and regeneration of dislocations). This issue has been examined in considerable detail in Nemat-Nasser et al. (1999) and Cheng and Nemat-Nasser (2001).

To examine the effect of temperature and strain rate on microstructural evolution, we have performed interrupted tests at two temperatures and two strain rates, for commercial Ti64. In Fig. 6(d), the heavy curves are the results of adiabatic tests; the dashed curves are the results of tests with a temperature jump, where the sample of an initial temperature 598 K is first loaded at a strain rate of 2000 s^{-1} to a true strain of 0.17. Then this sample is cooled to the temperature 391 K (i.e., 296 K + 95°C) and reloaded at the same strain rate of 2000 s^{-1}. The resulting dashed curve follows the adiabatic flow stress of a sample which has been loaded at the same strain rate, starting with the initial temperature of 296 K. With $\eta = 1$, Eq. (1) yields $\Delta T = 95$°C for 0.17 strain. The results of this temperature-jump test show that the microstructural changes corresponding to these temperature changes do not measurably affect the response of the sample. Fig. 7(a) displays the results of a strain rate jump. In

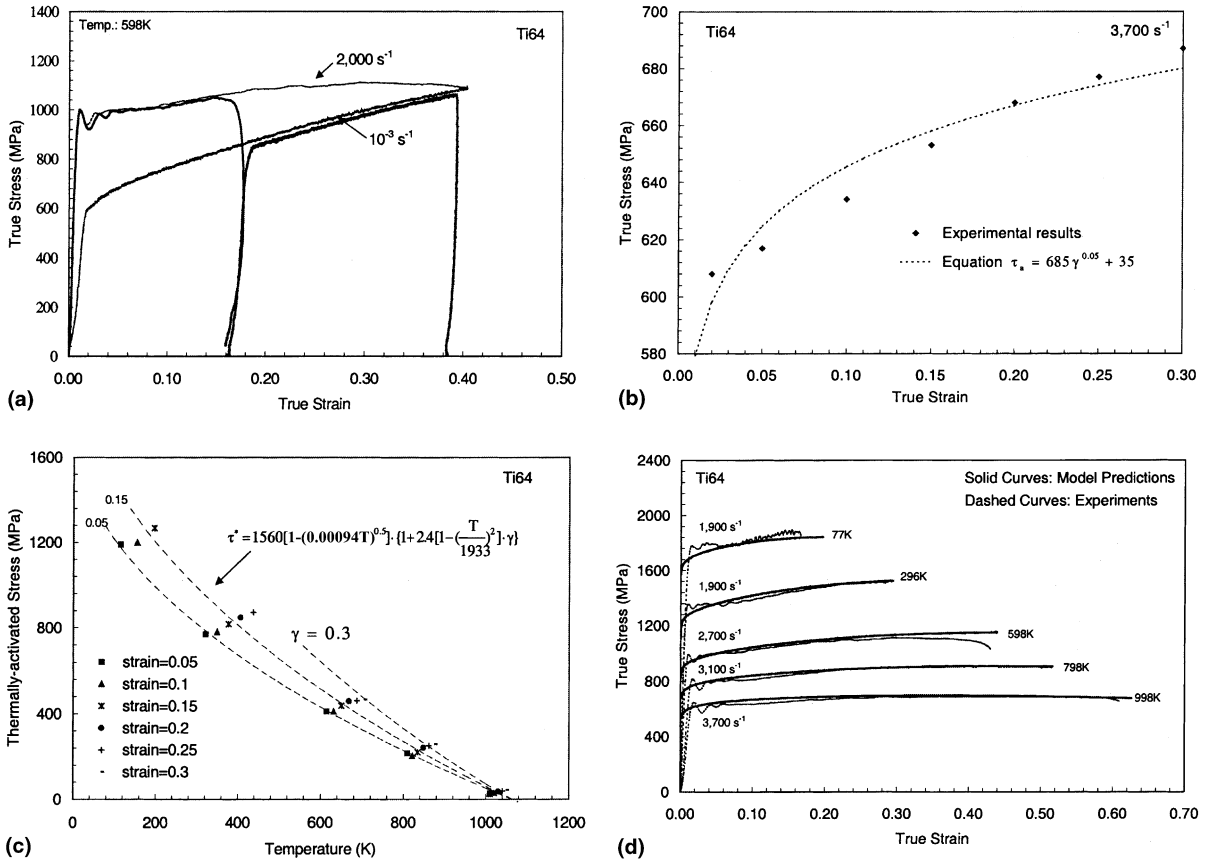

Fig. 7. (a) Interrupted tests for indicates strain rates; (b) athermal flow stress as a function of strain; (c) thermally activated flow stress as a function of temperature and strain at fixed strain rate; and (d) comparison of model predictions with actual experimetal results at indicated initial temperatures and strain rates.

this case, the sample is first loaded at a 2000 s^{-1} strain rate, unloaded, allowed to cool to its initial room temperature, and then reloaded at a strain rate 10^{-3} s^{-1}. The flow stress essentially follows the curve for the sample which has been loaded at a strain rate 10^{-3} s^{-1} from the beginning. The observed slight difference in the two curves, however, suggests the presence of some microstructural changes due to the changes in the strain rate and temperature.

5. Constitutive model

Several models have been used to formulate constitutive relations for Ti64. These include the Johnson–Cook model (Johnson and Cook, 1983), used by Lee and Lin (1998) for high strain rates and various temperatures; and the Mecking–Kocks model (Mecking and Kocks, 1981) used by Follansbee and Gray (1989). These models do not include the effect of dynamic strain aging.

If we focus our attention to a range of strain rates and temperatures, where dynamic strain aging is absent, then we may use the model proposed by Nemat-Nasser and Li (1997) for OFHC copper. In this model, the flow stress, τ, in uniaxial stress, is divided into two parts, one due to the athermal resistance to the motion of dislocations, denoted by τ_a, and the other associated with the thermally activated crossing of obstacles by dislocations, denoted by τ^*. Hence, $\tau = \tau^* + \tau_a$. In this work, we assume that τ_a depends on only the dislocation density ρ, while τ^* is both strain rate and temperature-dependent, as well as depending on ρ.

In most empirical models, the dependence of the flow stress on the dislocation density, ρ, is replaced by the dependence on the plastic strain, γ. While the dislocation density is related to the microstructural state of the material, the plastic strain may not be. On the other hand, because of the complex dislocation structure in polycrystalline solids, the farfield elastic stress field, produced by the dislocation forests, changes with the plastic straining. Hence, the corresponding athermal part, τ_a, of the flow stress also changes with the plastic strain. We shall, therefore, assume that τ_a is a function of ρ which itself is a function of the (monotonically increasing, since $\dot{\gamma} > 0$) strain measure, γ, i.e., $\tau_a = \tau_a(\rho(\gamma))$. As a simple model, we then represent τ_a as a power law in terms of γ, for the considered ranges of the strain rate and temperature. Using the experimental values of the flow stress at sufficiently high temperatures, where the flow stress is essentially temperature-independent, we have obtained the results shown in Fig. 7(b). In this figure, the dotted curve is obtained by a least-square fit, yielding $\tau_a = 685\gamma^{0.05} + 35$. However, as is seen from Fig. 6(b), tests results at temperatures greater than 1000 K are required in order to obtained accurate values of the athermal stress. We have found that the following approximation better fits the experimental results:

$$\tau_a = 685\gamma^{0.05}. \tag{2}$$

Now, following the procedure outlined by Nemat-Nasser and Isaacs (1997), we have plotted in Fig. 7(c), $\tau^* = \tau - \tau_a$, as a function of temperature for various indicated strains. As pointed out by Nemat-Nasser and Li (1997) and following Kocks et al. (1975) τ^* may be represented by

$$\tau^* = \hat{\tau}\left\{1 - \left[-\frac{kT}{G_0}\ln\frac{\dot{\gamma}}{\dot{\gamma}_r}\right]^{1/q}\right\}^{1/p}. \tag{3}$$

For dislocations as the short-range barriers, Nemat-Nasser and Li (1997) suggest the following expression for the stress:

$$\hat{\tau} = \frac{G_0}{b\lambda\ell} = \frac{G_0}{b\lambda\ell_0}\left(\frac{\ell_0}{\ell}\right) = \tau^0\frac{\ell_0}{\ell}, \tag{4}$$

and set

$$\dot{\gamma}_r = b\ell\rho_m\omega_0 = b\ell_0\rho_m\omega_0\frac{\ell}{\ell_0} = \dot{\gamma}_0\frac{\ell}{\ell_0}. \tag{5}$$

In the above equations, k is Boltzmann's constant; G_0 is the total energy barrier that a dislocation must overcome by its thermal activation in the absence of an applied stress; b is the magnitude of the Burgers vector; λ is the width of the energy barrier; ℓ_0 and ℓ are the initial (or some reference) and the current average dislocation spacing; ρ_m is the density of the mobile dislocations; and ω_0 is

the attempt frequency of a dislocation to overcome its energy barrier. In this formulation, it is assumed that the dislocation forest which intersects the slip plane forms the short-range energy barrier to the motion of dislocations which lie on the slip plane. Following Nemat-Nasser and Li (1997) and using our experimental results, we express ℓ_0/ℓ as follows:

$$\frac{\ell_0}{\ell} \approx f(\gamma, T) = 1 + a_0\left[1 - \left(\frac{T}{T_m}\right)^2\right]\gamma, \tag{6}$$

where T_m is the melting temperature (1933 K) and a_0 is a constant depending on the initial (or reference) dislocation density.

Combining Eqs. (3)–(5), we obtain the following explicit relation for τ^*:

$$\tau^* = 1560\left[1 - (0.00094T)^{1/2}\right] \times \left\{1 + 2.4\left[1 - \left(\frac{T}{1933}\right)^2\right]\gamma\right\}. \tag{7}$$

To relate (7) to model (3), it is necessary to estimate the values of G_0 and $\dot{\gamma}_0$ such that (7) holds. De Meester et al. (1975) have suggested $G_0 \approx 1.3$ eV for Ti64 at temperatures 4.2–760 K, and Okazaki et al. (1974) have proposed $G_0 \approx 1.4$ eV for Ti–7.4 at.% Al at temperatures 77–700 K. Here we take $G_0 \approx 1.4$ eV which yields $k/G_0 = 6.2 \times 10^{-5}$ K^{-1}. Then, with $b \approx 2.8 \times 10^{-5}$ cm, $\omega_0 = \mathrm{O}(10^{11}\ \mathrm{s}^{-1})$ [32], $\rho_m = \mathrm{O}(10^{11}\ \mathrm{cm}^2)$, and assuming ℓ_0 to be about 500 lattice spacing, we obtain $\dot{\gamma}_0 = 1.32 \times 10^{10}\ \mathrm{s}^{-1}$. Finally, constitutive equation for Ti64 becomes

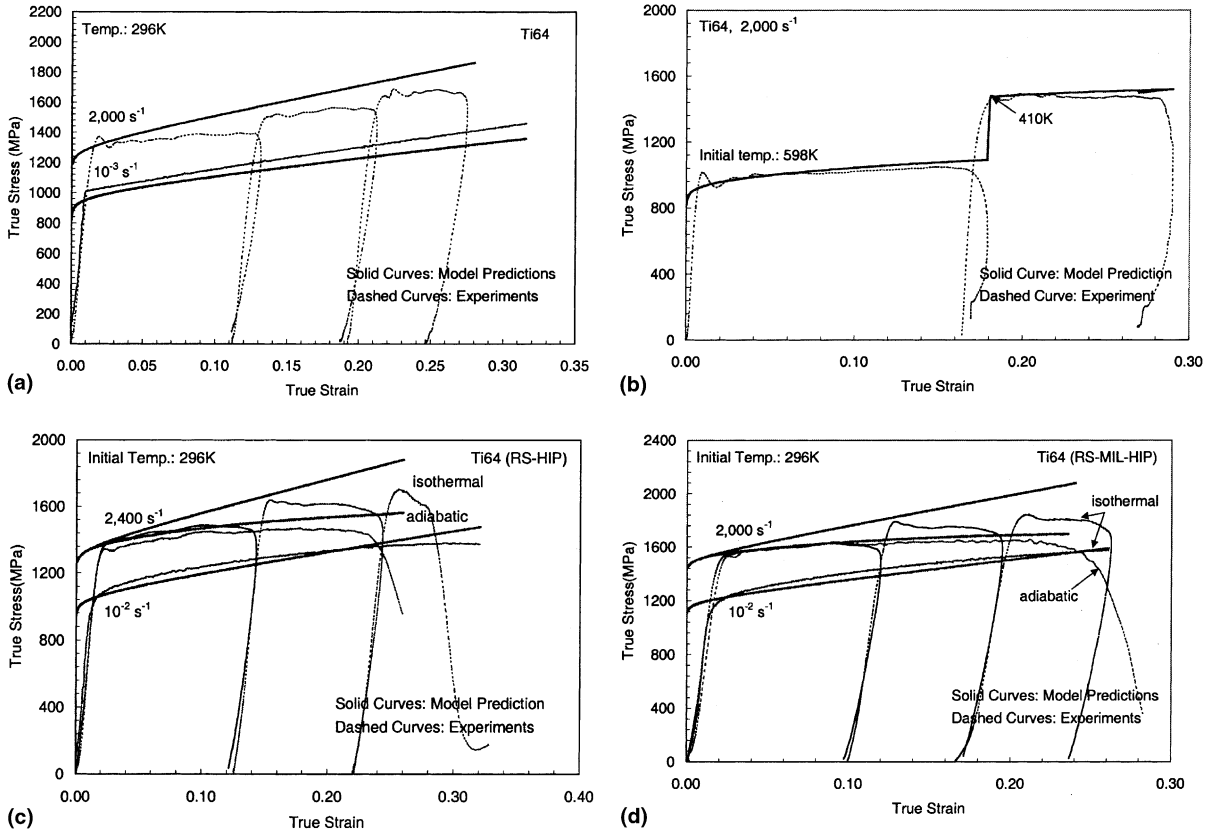

Fig. 8. Comparison of models predictions with experimental results: (a) and (b) for commercial Ti64, (c) for RS-HIP Ti64, and (d) for RS-MIL-HIP Ti64 at indicated initial temperatures and strain rates.

$$\tau = 685\gamma^{0.05} + 1560\left\{1 - \left[-6.210^{-5}T\left(\ln\frac{\dot{\gamma}}{1.32\times10^{10}} + \ln f(\gamma,T)\right)\right]^{0.5}\right\} f(\gamma,T),$$

$$f(\gamma,T) = 1 + 2.4\left[1 - \left(\frac{T}{1933}\right)^2\right]\gamma, \tag{8}$$

where the temperature is calculated from

$$T = T_0 + \Delta T,$$
$$\Delta T = \int_0^\gamma \frac{\tau}{4.39C_V}\,\mathrm{d}\gamma, \tag{9}$$
$$C_V = 0.56\exp(T/2000).$$

Fig. 7(d) compares the results obtained from Eqs. (8) and (9) with the experimental results, for indicated strain rates and initial temperatures. In Fig. 8(a) the isothermal predictions of the model are compared with the corresponding experimental results for indicated strain rates. Fig. 8(b) compares the experimental and model results of a temperature-jump test.

With above these results, the general constitutive relation for Ti64 is as follows:

$$\tau = \tau_a^0\gamma^n + \tau^0\left\{1 - \left[\frac{k}{G_0}T\left(\ln\frac{\dot{\gamma}f(\gamma,T)}{\dot{\gamma}_0}\right)\right]^{1/2}\right\} f(\gamma,T) \tag{10}$$

$$f(\gamma,T) = 1 + a_0\left[1 - \left(\frac{T}{T_m}\right)^2\right]\gamma.$$

As pointed out in Section 1, the initial microstructure (including grain sizes and their distribution) only affects the athermal part of the flow stress. We have applied Eqs. (9) and (10) to RS-HIP and RS-MIL-HIP Ti64 by only adjusting the three parameters, τ_a^0, n, and τ^0. The results are displayed in Fig. 8(c) and (d), with the values of the model parameters given in Table 2. Model predictions are in good agreement with the experimental results.

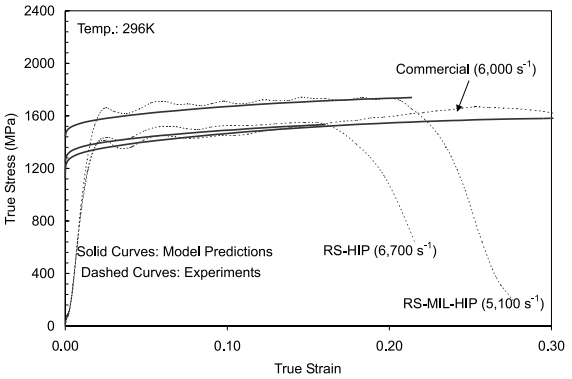

Fig. 9. Comparison of model predictions with experimental results under higher strain rates.

In addition, we have performed experiments at strain rates of about 6000 s^{-1} and an initial temperature of 296 K, for all three materials. These experimental results are used to independently verify the model predictions. The data and the corresponding model predictions are shown in Fig. 9. Again, good agreement between experimental and model results is obtained.

6. Conclusions

In the present work, the dynamic thermomechanical response of Ti64 alloys with three different microstructures is systematically studied over a broad range of temperatures and strain rates. A physically based model is developed to predict the

Table 2
Values of various constitutive parameters for the three Ti64 materials

Parameter	p	q	k/G_0 ($\times10^{-5}$ K^{-1})	$\dot{\gamma}_0$ ($\times10^{10}$ s^{-1})	a_0	τ^0	τ_a^0	n
Commercial Ti64	1	2	6.2	1.32	2.4	**1560**	**685**	**0.05**
RS-MIL-HIP Ti64	1	2	6.2	1.32	2.4	**1900**	**710**	**0.03**
RS-HIP Ti64	1	2	6.2	1.32	2.4	**1620**	**680**	**0.04**

flow response of these three materials. Major conclusions are as follows:

1. Experimental results show that, RS-MIL-HIP Ti64 has higher flow strength than RS-HIP and the commercial Ti64. The flow stress in RS-HIP Ti64 is close to that of the commercial Ti64. Both RS-MIL-HIP and RS-HIP Ti64 is shown lower ductility than the commercial Ti64.
2. Microstructural examination reveals that, adiabatic shearbands and the associated fracture are the main failure characteristics of Ti64 at high strain rates and low temperatures. Depending on the test temperature, shearbands develop once a sample is deformed to suitably large strains.
3. For all three materials, the flow stress is more sensitive to the temperature of the material than to the strain rate.
4. In the absence of dynamic strain aging, the constitutive model presented in this paper for Ti64 seems to fit the experimental results over a broad range of temperatures and strain rates.
5. Comparing the results for the three Ti64 alloys, it is found that, the initial microstructural features affect only the magnitude of the threshold stress and the athermal part of the flow stress, but not the functional dependence of the thermally activated part of the flow stress on the temperature and the strain rate.

Acknowledgements

The authors would like to express their appreciation to Mr. Jon Isaacs for his assistance in performing the experiments. This work has been supported by the ARO MURI under contract DAAH04-96-1-0376 (Program Manager, Dr. David Stepp) with the University of California, San Diego.

References

ASM Committee on Titanium and Titanium Alloys, 1980. Metals Handbook, vol. 3, ninth ed. ASM International, Metals Park, OH, pp. 389.

Boyer, R., Welsch, G., Collings, E.W. (Eds.), 1994. Materials Properties Handbook: Titanium Alloys: Ti–6Al–4V. ASM International, Materials Park, OH, pp. 483–617.

Burkins, M., Love, W., 1996. Effect of annealing temperature on the ballistic limit velocity of Ti–6Al–4V ELI. In: Proceedings of the 16th International Symposium on Ballistics. San Francisco, pp. 723–732.

Cheng, J.Y., Nemat-Nasser, S., 2001. A model for experimentally-observed high-strain-rate dynamic strain aging in titanium. Acta Mater. 48, 3131–3144.

Cottrell, A.H., Jaswon, M.A., 1949. Distribution of solute atoms round a slow dislocation line. Proc. Roy. Soc. A 199, 104–114.

De Meester, B., Doner, M., Conrad, H., 1975. Deformation kinetics of the Ti–6Al–4V alloy at low temperatures. Metall. Trans. A 6, 65–74.

Doner, M., Conrad, H., 1973. Deformation mechanisms in commercial Ti-50A (0.5 at.% O_{eq}) at intermediate and high temperatures ($0.3–0.6T_m$). Metall. Trans. 4, 2809–2817.

Follansbee, P.S., Gray III, G.T., 1989. An analysis of the low-temperature, low and high strain-rate deformation of Ti–6Al–4V. Metall. Trans. A 20, 863–874.

Grebe, H.A., Pak, H-R., Meyers, M.A., 1985. Adiabatic shear localization in titanium and Ti–6%Al–4%V alloy. Metall. Trans. A 16, 761–775.

Johnson, G.R., Cook, W.H., 1983. In: Proceedings of the 7th International Symposium on Ballistics. KIVI, The Hague, Netherlands, p. 541.

Kailas, S.V., Prasad, Y.V.R.K., Biswas, S.K., 1994. Flow instabilities and fracture in Ti–6Al–4V deformed in compression at 298 K to 673 K. Metall. Trans. A 25, 2173–2179.

Kapoor, R., Nemat-Nasser, S., 1998. Determination of temperature rise during high strain rate deformation. Mech. Metall. 27, 1–12.

Keh, A.S., Nakada, Y., Leslie, W.C., 1968. In: Rosenfield, A.R., Hahn, G.T., Bement, A.L., Jaffee, R.I. (Eds.), Dislocation Dynamics. McGraw-Hill, New York, pp. 381–408.

Kerr, W.R., 1985. The effect of hydrogen as a temporary alloying element on the microstructure and tensile properties of Ti–6Al–4V. Metall. Trans. A 16, 1077–1087.

Kocks, U.F., Argon, A.S., Ashby, M.F., 1975. In: Chalmers, B., Christian, J.W., Massalski, T.B. (Eds.), Progress in Materials Science, vol. 19, Thermodynamics and Kinetics of Slip. Pergamon Press, Oxford, pp. 120–129.

Lee, W.-S., Lin, C.-F., 1998. Plastic deformation and fracture behaviour of Ti–6Al–4V alloy loaded with high strain rate under various temperatures. Mater. Sci. Eng. A 241, 48–59.

Liu, Y., Nesterenko, V.F., Indrakanti, S.S., 1998. Modified Arzt–Ashby–Easterling model for powder consolidation. Met. Mater. 4, 336–344.

Makel, D.D., Eylon, D., 1990. The effect of microstructure on localized melting at separation in Ti–6Al–4V tensile samples. Metall. Trans. A 21, 3127–3136.

McDarmaid, D.S., Partridge, P.G., 1986. The effect of strain rate, temperature and texture on anisotropic deformation in Ti–6Al–4V. J. Mater. Sci. 21, 1525–1532.

Me-Bar, Y., Rosenberg, Z., 1997. On the correlation between the ballistic behavior and dynamic properties of titanium-alloy plates. Int. J. Impact Eng. 19, 311–318.

Me-bar, Y., Shechtman, D., 1983. On the adiabatic shear of Ti–6Al–4V ballistic targets. Mater. Sci. Eng. 58, 181–188.

Mecking, H., Kocks, U.F., 1981. Kinetics of flow and strain-hardening. Acta Metall. 29, 1865–1875.

Montgomery, J.S., Wells, M.G.H., Roopchand, B., Ogilvy, J.W., 1997. Low-cost titanium armors for combat vehicles. JOM, 45–47.

Nemat-Nasser, S., Guo, W.G., Cheng, J.Y., 1999. Mechanical properties and deformation mechanisms of a commercially pure titanium. Acta Mater. 47, 3705.

Nemat-Nasser, S., Isaacs, J.B., 1997. Direct measurement of isothermal flow stress of metals at elevated temperatures and high strain rates with application to Ta–W alloys. Acta Mater. 45, 907–919.

Nemat-Nasser, S., Isaacs, J.B., Starrett, J.E., 1991. Hopkinson techniques for dynamic recovery experiments. Proc. R. Soc. 435, 371–391.

Nemat-Nasser, S., Li, Y.F., Isaacs, J.B., 1994. Experimental computational evaluation of flow-stress at high-strain rates with application to adiabatic shear banding. Mech. Mater. 17, 111–134.

Nemat-Nasser, S., Li, Y.L., 1997. Flow stress of F.C.C. ploycrystals with application to OHFC Cu. Acta Mater. 46, 565–577.

Nesterenko, V.F., Indrakanti, S.S., Brar, S., Gu, Y., 2000. In: Furnish, M.D., Chhabildas, L.C., Hixson, R.S. (Eds.), Proceedings of the 11th Biennial International Conference of the American Physical Society – Shock Compression of Condensed Matter. AIP, pp. 419–422.

Okazaki, K., Itoh, T., Conrad, H., 1974. The effect of grain size on the strength of a Ti–7.4 at%Al alloy at low temperatures. Trans. JIM 15, 159–166.

Reed-Hill, R.E., Iswaran, C.V., Kaufman, M.J., 1996. An analysis of the flow stress of a two-phase alloy system Ti–6Al–4V. Metall. Mater. Trans. A 27, 3957–3962.

Williams, S.C., 1965. Report on Titanium: The Ninth Industrial Metal. Edwards Brothers, Ann Arbor, pp. 160–164.